11-8-2018

In Vivo Extracellular pH Mapping of Tumors Using Electron Paramagnetic Resonance

Denis A. Komarov
Hokkaido University

Yuki Ichikawa
Hokkaido University

Kumiko Yamamoto
Hokkaido University

Neil J. Stewart
Hokkaido University

Shingo Matsumoto
Hokkaido University

See next page for additional authors

Published in final edited form as:

Anal Chem. 2018 December 04; 90(23): 13938–13945. doi:10.1021/acs.analchem.8b03328.

In vivo extracellular pH mapping of tumors using electron paramagnetic resonance

Denis A. Komarov[†,¶], **Yuki Ichikawa**[†], **Kumiko Yamamoto**[‡], **Neil J. Stewart**[†], **Shingo Matsumoto**[†], **Hironobu Yasui**[§], **Igor A. Kirilyuk**[‖], **Valery V. Khramtsov**[⊥], **Osamu Inanami**[‡], and **Hiroshi Hirata**[*,†]

[†]Division of Bioengineering and Bioinformatics, Graduate School of Information Science and Technology, Hokkaido University, North 14, West 9, Kita-ku, Sapporo, 060-0814, Japan

[‡]Laboratory of Radiation Biology, Graduate School of Veterinary Medicine, Hokkaido University, North 18, West 9, Kita-ku, Sapporo, 060-0818, Japan

[§]Central Institute of Isotope Science, Hokkaido University, North 15, West 7, Kita-ku, Sapporo, 060-0815, Japan

[‖]N. N. Vorozhtsov Novosibirsk Institute of Organic Chemistry, 9, Ac. Lavrentieva Ave., Novosibirsk, 630090, Russia

[⊥]Department of Biochemistry, and In Vivo Multifunctional Magnetic Resonance center, West Virginia University, Robert C. Byrd Health Sciences Center, 1 Medical Center Drive, Morgantown, West Virginia 26506, USA

Abstract

An electron paramagnetic resonance (EPR) based method for noninvasive three-dimensional extracellular pH mapping was developed using a pH-sensitive nitroxyl radical as an exogenous paramagnetic probe. Fast projection scanning with a constant magnetic field sweep enabled the acquisition of four-dimensional (3D spatial + 1D spectral) EPR images within 7.5 min. Three-dimensional maps of pH were reconstructed by processing the pH-dependent spectral information of the images. To demonstrate the proposed method of pH mapping, the progress of extracellular acidosis in tumor-bearing mouse legs was studied. Furthermore, extracellular pH mapping was used to visualize the spatial distribution of acidification in different tumor xenograft mouse models of human-derived pancreatic ductal adenocarcinoma cells. The proposed EPR-based pH mapping method enabled quantitative visualization of changes in extracellular pH due to altered tumor metabolism.

[*]**Corresponding Author:** hhirata@ist.hokudai.ac.jp.

[¶]**Present Address:** D.A.K.: Davis Heart and Lung Research Institute, The Ohio State University, Columbus, Ohio 43210, USA.

Author Contributions

The manuscript was written with contributions from all authors. All authors have given approval to the final version of the manuscript.

ASSOCIATED CONTENT

Supporting Information

The Supporting Information is available free of charge on the ACS Publications website.

Experimental details of cytotoxicity assay, animal preparation and tumor models, and Figures S1–S5 (PDF).

Notes

The authors declare no competing financial interest.

Graphical Abstract

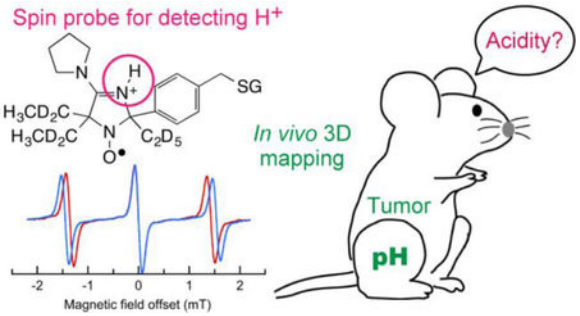

Keywords

3D extracellular pH mapping; electron paramagnetic resonance; tumor microenvironment; acidification; tumor xenografts

Glucose metabolism is altered in cancer cells,[1] and extracellular acidosis due to metabolic changes is a hallmark of tumor microenvironment.[2] Since low extracellular pH (pH_e) affects tumor progression and susceptibility to chemotherapy,[3] extracellular acidosis has received considerable attention from oncology clinicians and researchers. In light of this, accurate *in vivo* monitoring of pH_e is undoubtedly desirable for the study of cancer pathology and the development of new therapeutic strategies. Several methods for imaging pH in tumor tissues have been developed,[4] such as fluorescence-based pH mapping,[5] ^{31}P-nuclear magnetic resonance (NMR),[6,7] chemical exchange saturation transfer magnetic resonance imaging (CEST-MRI),[8] MRI of hyperpolarized ^{13}C-labeled bicarbonate and zymonic acid,[9,10] and proton-electron double resonance imaging (PEDRI).[11,12] However, as yet there is no accepted gold standard for non-invasive pH_e mapping of tumors in a preclinical or clinical setting.

While electron paramagnetic resonance (EPR) spectroscopy has previously been used with a pH-sensitive spin probe for *in vivo* measurements of pH in small animals,[13–18] extension of those spectroscopic measurements to three-dimensional (3D) pH mapping in animal models using EPR is practically challenging. A major challenge of EPR-based 3D pH mapping is the longer acquisition time associated with four-dimensional (4D) EPR imaging that comprises 3D spatial and one-dimensional (1D) spectral data. Acquisition of a sufficient number of EPR spectral projections for adequate reconstruction is a critical obstacle in 3D pH mapping. Moreover, precise reconstruction of EPR spectra at the level of each voxel is essential for pH mapping with reasonable accuracy, e.g., less than 0.1 pH units. This requires improvement of existing techniques for estimation of pH from EPR spectral lineshapes, in conjunction with a robust 4D image reconstruction.

In this work, we report an EPR-based method for *in vivo* 3D mapping of extracellular pH in mouse tumor models. This was achieved using a home-built continuous-wave (CW)-EPR imager capable of fast projection scanning,[19,20] in combination with a pH-sensitive nitroxyl probe. The probe was specifically designed for extracellular pH measurements *in vivo*[11] and is highly water soluble and non-toxic. The *in vivo* lifetime is sufficiently long (~20 min) to

perform a 4D EPR acquisition. Four-dimensional EPR images were reconstructed using an optimized iterative reconstruction algorithm,[21] in conjunction with a novel procedure for the fitting of spectral data to improve reconstruction convergence to a stable solution. By this method, low-noise EPR images could be obtained even for acquired projections with a relatively low signal-to-noise ratio. We demonstrated the proposed method of 3D pH_e mapping by measuring the progress of extracellular acidosis in tumor-bearing mouse legs. Furthermore, different spatial distributions of acidification were visualized for several different tumor xenograft mouse models using human-derived pancreatic cancer cells.

EXPERIMENTAL SECTION

Chemicals.

The pH-sensitive nitroxyl radical 2-(4-((2-(4-amino-4-carboxybutanamido)-3-(carboxymethylamino)-3-oxoproylthio)methyl)phenyl)-4-pyrrolidino-2,5,5-triethyl-2,5-dihydro-1H-imidazol-1-oxyl (R-SG, Fig. 1A, X = H; Y=CH_3) and its deuterium-enriched analog (dR-SG, Fig. 1A, X = D; Y=CH_3 (1/3); CD_3 (2/3)) were synthesized as previously reported.[11,12]

EPR imager.

A home-built CW-EPR spectrometer/imager operating at 750 MHz was used for spectroscopy and imaging. Details of the EPR instrumentation have been reported previously.[19,20] In brief, a permanent magnet of 27 mT was used with three pairs of gradient coils and a pair of field scanning coils. A multi-coil parallel-gap resonator (22 mm diameter, 30 mm length) and a reflection-type RF bridge were used for EPR detection.[19,22]

In vitro pH mapping.

The pH-sensitive nitroxyl radical R-SG, 2 mM, was dissolved in phosphate-buffered saline (PBS). Three radical solutions with pH 6.60, 6.80, and 7.00 were prepared by adding the necessary amount of HCl. The solution pH was measured using a pH meter (pH1500, Eutech Instruments, Singapore, manufacture verified accuracy ± 0.05 pH units) equipped with a glass electrode (InLab Semi-Micro, Mettler Toledo, Columbus, OH). The pH meter was calibrated using standard pH buffer solutions [ECBU4BT (4.01 pH units), ECBU7BT (7.00 pH units), and ECBU10BT (10.01 pH units), Thermo Fisher Scientific, Inc., Singapore]. This calibration process ensured that the prepared radical solutions could be pH-references with a best possible accuracy equal to that of the pH meter.

The solutions were placed into flame-sealed glass tubes with 5.3 mm inner diameter. In each case, the approximate volume of radical solution was 0.7 mL. The tubes were placed in a plastic holder made of cross-linked polystyrene, Rexolite 1422 (C-Lec Plastics Inc., Philadelphia, PA) and transferred to the resonator of the 750-MHz CW-EPR imager. The following measurement settings were used for EPR image acquisition: scan time 0.1 s, scanning magnetic field 9.0 mT, magnetic field modulation 0.2 mT, modulation frequency 90 kHz, lock-in amplifier time-constant 100 μs, number of data points 2048 per scan, and incident RF power 2.2 mW. All EPR projections were recorded with a constant sweep of the magnetic field.[21] Incrementally-ramped field gradients were used for EPR image

acquisition. The projections were acquired at 15 × 15 × 15 field gradients for the X-, Y-, and Z-directions (total of 3375 projections). The maximum field gradient for each direction was 70 mT/m. The total acquisition time was 7.5 min. The pH mapping of the three radical solutions was performed at room temperature (25 ºC).

In vivo pH mapping.

For *in vivo* pH mapping of tumor-bearing mouse legs, the pH-sensitive nitroxyl radical dR-SG was dissolved in pure water (to make a concentration of 100 mM), and the solution pH was adjusted to 7.4 by the addition of NaOH. Mice were anesthetized by inhalation of 1.5–2.0% isoflurane and the tail vein was cannulated. Mice were then placed on a plastic holder made of Rexolite 1422 and transferred to the CW-EPR imager with the tumor-bearing leg positioned at the center of the resonator. The mouse body temperature and respiration rate were continuously monitored using a small animal monitoring and gating system (model 1030, SA Instruments, Inc., Stony Brook, NY). Body temperature was maintained at 36 to 37ºC by a feedback-regulated heated airflow system. During the EPR measurements, isoflurane anesthesia was maintained at 1.0–1.5%. The dR-SG radical (10 mg, 0.6 mmol/kg body weight) was intravenously injected as a bolus over the course of 30 s through the tail vein catheter. Tumor model mice were weighed at 22 to 24 g at the time of experiment. EPR acquisition was started two minutes after the injection. The EPR settings for imaging of tumor-bearing mice were the same as those for imaging the solution samples, except for incident RF power, 11.5 mW, modulation amplitude, 0.15 mT, and lock-in amplifier time constant, 30 μs. All experiments were performed under the ‘Law for The Care and Welfare of Animals in Japan’ and were approved by the Animal Experiment Committee of Hokkaido University (approval no. 15–0120).

Image reconstruction and spectral data fitting.

Four-dimensional spectral-spatial EPR images were reconstructed by an algebraic reconstruction technique (ART), with spectral data fitting at each iteration. All computations were performed on an Apple iMac computer (Mid 2010, Intel Core i3, 3 GHz, memory 4 GB). The reconstruction procedure was implemented in MATLAB (MathWorks, Natick, MA) with an ART algorithm written in C-language for speed and compiled as a MATLAB-executable (MEX) function. Full details of the reconstruction algorithm were reported previously.[21] 4D EPR images were reconstructed to a matrix size of 768 × 48 × 48 × 64 points, corresponding to a spectral window of 6.75 mT and field-of-view of 25 mm × 25 mm × 33.3 mm for the pH phantom, and to a matrix size of 768 × 48 × 48 × 48 points, corresponding to a spectral window of 6.75 mT and field-of-view of 25 mm × 25 mm × 25 mm for *in vivo* tumor-bearing mouse legs. After each ART iteration, the spatial data were smoothed using a 3D Gaussian filter with a standard deviation of 0.8 pixels (corresponding to a full-width at half maximum (FWHM) of 1 mm, i.e., best-case spatial resolution). However, this Gaussian filter does not necessarily affect the spatial resolution when the FWHM of the Gaussian filter is sufficiently less than the experimentally-defined spatial resolution of the mapping method, which is mainly governed by the peak-to-peak linewidth of the probe and the applied magnetic field gradient (see Results and Discussion sections).

For the fitting of spectral data, calibration sets of EPR spectra for both R-SG and dR-SG radicals were recorded over a pH range of 3 to 10, with an interval of 0.2 pH units around the pK_a value (Fig. S1). Deuteration of the probe does not affect the hyperfine splitting and the process of pH estimation; the hyperfine splitting structure of both probes is constant for both probes in the range of room temperature to 37 ºC, but it is worth noting that dR-SG has narrower peak-to-peak EPR absorption peaks than R-SG.[11,12,25] The spectral data of the images were fitted by a linear combination of the spectra from the corresponding calibration set. To fit the spectral data of an EPR image and generate the pH map, first, an averaged EPR spectrum for the whole sample was calculated by summing the spectral data of the image. The central line of the averaged spectrum was fitted with a Voigt profile to calculate its position on the spectral coordinate. Note, the central line of the R-SG and dR-SG spectra does not change with pH, and its position solely depends on the loading of the EPR resonator and the spectrometer settings. Using the calculated position of the central EPR line, the spectra from the calibration set (Fig. S1) were shifted to the correct field position by multiplication with a corresponding phase multiplier in the Fourier domain:

$$\mathrm{DFT}\left[\boldsymbol{B}_i(H+\Delta H)\right] = e^{-2\pi i \Delta H \xi}\mathrm{DFT}\left[\boldsymbol{B}_i(H)\right], \quad (1)$$

where DFT is the discrete Fourier transform, i is a spectrum from the calibration set, H is the magnetic field, ΔH is the difference in the magnetic field for the averaged image spectrum and the spectra from the calibration set, and ξ is the Fourier domain frequency variable.

Then, for each voxel of the 4D EPR image, the spectrum from the calibration set, $\boldsymbol{B}_i$ which best describes the observed spectrum, $\boldsymbol{E}$, was determined by solving the equation for the linear coefficient, c_i, and finding the minimum of the residual sum of squares, RSS, defined as follows:

$$c_i = \frac{\boldsymbol{B}_i \cdot \boldsymbol{E}}{\boldsymbol{B}_i \cdot \boldsymbol{B}_i}, \quad (2)$$

$$RSS = \left\| \boldsymbol{E} - c_i \boldsymbol{B}_i \right\|. \quad (3)$$

After finding the closest-matching spectrum $\boldsymbol{B}_i$, the observed spectrum, $\boldsymbol{E}$, was fitted by the linear combination of $\boldsymbol{B}_i$ and its two neighboring spectra, with a non-negative constraint:

$$\boldsymbol{E} \approx a_{i-1}\boldsymbol{B}_{i-1} + a_i \boldsymbol{B}_i + a_{i+1}\boldsymbol{B}_{i+1}. \quad (4)$$

Finally, the pH value of the voxel was calculated according to the formula:

$$\mathrm{pH} = \mathrm{pK_a} + \log_{10}\frac{\sum a_i[R]_i}{\sum a_i[RH^+]_i}, \quad (5)$$

where $[RH^+]_i$ and $[R]_i$ are the known concentrations of protonated and unprotonated forms of the radical for each particular calibration solution. The pK_a for the R-SG (and dR-SG) radical was 6.84 at 23 ºC and 6.60 at 37 ºC.[11] Since *in vitro* pH mapping was performed at room temperature (25 ºC), we set pK_a at 6.80 pH units. Since evidence that the sample temperature does not affect the hyperfine splitting constants of R-SG and dR-SG was previously reported,[11,12,25] we did not take a shift in the hyperfine splitting constants into account for the different temperatures used for *in vitro* and *in vivo* experiments in our study.

In this approach, the method for solving the linear equations (eq. 4) was employed to obtain the approximation of the whole spectral line-shape at each voxel. Our method is close to the concept of the “matching pursuit” algorithm for obtaining an approximation of the whole spectral line-shape. This method should be distinguished from a previous method reported by our laboratory, in which the apparent hyperfine splitting constant for three-line EPR absorption peaks was measured to determine pH values;[23] in the present study, no hyperfine splitting constant measurement was performed.

Functional resolution and accuracy.

For solution samples, functional resolution of pH measurements was defined as the full-width at half maximum (FWHM) of the normal curve that reflects the probability density of pH values at each voxel:

$$\mathrm{FWHM} = 2SD\sqrt{2\log_e 2} = 2.35\,SD, \quad (6)$$

where *SD* is the standard deviation of measured pH values at each voxel. In this estimation, we assumed the normal distribution for pH values at each voxel. After computing the *SD*s of pH values in each solution sample, FWHMs were calculated. In our experiments, we defined the functional resolution of pH measurements as the mean of the three FWHMs corresponding to the three sample tubes. This functional resolution effectively corresponds to the “precision” of pH measurements, i.e., the closeness of agreement between pH values at each voxel. Moreover, the accuracy, i.e., trueness of pH measurements was defined as the closeness of agreement between the average pH value obtained from each voxel and the reference value, which is the known pH value of the corresponding sample solution in our case. In this study, we estimated the accuracy of pH measurements for the three solution samples as the mean of the differences between the average pH values of each tube obtained by EPR-based pH mapping and the reference pH values (6.60, 6.80, and 7.00 pH units) measured by a commercial pH meter, as mentioned above.

Magnetic resonance imaging.

MRI was performed on a home-built 1.5 T permanent magnet system, using a home-built ^{1}H mouse body coil and a dedicated spectrometer (MR Solutions, Guildford, UK). The same mouse bed was used for both EPR and MRI to ensure approximately equivalent scan positioning and facilitate image registration. A 2D T_2-weighted fast spin echo sequence was used for anatomical imaging of the tumor-bearing leg. Sequence parameters were as follows: field-of-view (FOV) 32 mm × 32 mm; 128 × 128 in-plane matrix; 32 slices of thickness 2 mm, overlap 1mm; echo/repetition time (TE/TR) 68/4876 ms; echo train 8; number of averages 3; scan time ~4 min. 2D scans were acquired in all three anatomical planes to permit reconstruction of arbitrary slices for accurate spatial comparison with the 3D EPR imaging data. Tumor volume was evaluated from MRI by selecting the tumor region on sagittal-plane images.

Statistical analysis.

To compare the mean values of the median pH_e of tumor-bearing mice, a two-tailed paired *t*-test was used. The sample size of tumor-bearing mice ($n = 7$) was selected based on previously reported pH_e data of SCC VII tumor-bearing mice,[23] in which the change in the mean pH_e for the tumor-bearing legs between day 5 and 8 was 0.12 pH units and the standard deviation of a single pH measurement was 0.076 pH units. Using these values and choosing the level of Type I error $\alpha = 0.05$ and Type II error $\beta = 0.2$ for pH measurements yielded a required sample size of 7.[24] For the animal study of pH_e mapping during tumor growth, randomization was not used and no blinding was done because of the paired nature of the experiment.

RESULTS

3D pH mapping with solution samples.

We used an imidazoline nitroxyl radical bound with glutathione (R-SG, see Fig. 1a for the structure) as a spin probe for pH measurements by EPR.[11,25,26] This radical probe shows a pH-dependent EPR spectrum with different hyperfine splitting constants for protonated and unprotonated forms as shown in Fig. 1b (also see Supporting Information Fig. S1 for EPR spectra at various pH values). The pK_a value of the radical is 6.60 at 37 °C which is suitable for pH measurements in the normal physiological range and slightly acidic conditions.

The proposed method of 3D pH mapping was experimentally verified using a solution phantom consisting of three glass tubes with 2 mM R-SG solutions at pH 6.60, 6.80, and 7.00. Fig. 2a shows a photograph of the phantom. We performed 4D EPR imaging with a total data acquisition time of 7.5 min. After image reconstruction and spectral data fitting, 3D maps of EPR signal intensity and pH were obtained. Fig. 2b shows a surface-rendered image of the EPR signal distribution that accurately reflects the geometry of the solution phantom. Figs. 2c and 2d show corresponding maps of the EPR signal intensity and pH for the cross-sectional slice shown at the center of Fig. 2b, respectively. Fig. 2e shows the histograms of pH values for each of the three tubes. The measured pH values were 6.591 ± 0.025, 6.839 ± 0.035 and 7.029 ± 0.039 (mean ± standard deviation), which well reproduced the real pH values. From the calculated standard deviations above, functional

resolution, i.e., precision of pH measurements was estimated to be 0.078 pH units, according to its definition in the Experimental Section. The accuracy of pH measurements was estimated to be 0.026 pH units, which is less than the precision of the commercial pH-meter we used for pH calibration.

By fitting the signal distributions in Fig. 2c with a Gaussian function, the spatial resolution of pH maps was determined to be 3 mm. In practice, the spatial resolution of an EPR imaging experiment depends on the width of the spectral line and the applied magnetic field gradient. The gradient is typically limited by the signal-to-noise ratio of acquired EPR projections. In our case, the maximum gradient of the magnetic field was 70 mT/m, and the peak-to-peak linewidth of the R-SG probe was 0.21 mT. Thus, the spatial resolution can be estimated as linewidth/gradient = 3 mm, which accurately repeats the Gaussian fitting result given above.

Extracellular acidosis during tumor growth.

In vivo EPR-based pH mapping was demonstrated using tumor-bearing mice. The progress of acidification in murine squamous cell carcinoma (SCC VII) cells implanted into the right hind legs of mice was monitored. (Full details of animal preparation are given in Supporting Information.) To increase the sensitivity of EPR measurements and achieve a better spatial resolution, the deuterated radical dR-SG (Fig. 1a) was used for *in vivo* pH mapping. The deuterated radical dR-SG has an EPR linewidth of about 0.12 mT. However, in this work the projections were recorded with a modulation amplitude of 0.15 mT (rather than 0.2 mT as for solution samples) to achieve a better signal-to-noise ratio. Therefore, we estimate that the spatial resolution of the *in vivo* measurements was ~2 mm. In addition, an *in vitro* cytotoxicity test for R-SG (see Supporting Information, Fig. S2) showed that 56% of HeLa cells survived when incubated with 10 mM R-SG for 4 days.

Fig. 3a shows a photograph of the leg of an SCC VII tumor-bearing mouse placed on a plastic holder for EPR measurements. The dashed lines indicate the region visualized by EPR imaging. Fig. 3b shows surface-rendered EPR images of the leg (and part of the tail) of a mouse measured at 5 and 8 days after tumor implantation. Figs. 3c and 3d show T_2-weighted anatomical MR images for the sagittal plane on day 5 and 8, respectively. The corresponding maps of the EPR signal intensity are given in Figs. 3e and 3f. The positions of the maps are shown in Fig. 3b with dashed lines. Both MR and EPR images demonstrated enlargement of the tumor over time. Also, the EPR images revealed a low-signal-intensity area in the center of the tumor that presumably appeared due to insufficient delivery of the spin probe to the relatively poorly perfused tumor tissue. The size of the low-intensity area significantly increased on day 8 compared with day 5.

Extracellular pH was visualized for the tumor-bearing leg in 3D. Figs. 3g (day 5) and 3h (day 8) present the maps of pH_e in the sagittal plane corresponding to the EPR signal intensity maps in Figs. 3e and 3f. Masks generated from MR anatomical images were applied to remove pH data outside the leg. The maps of pH_e obtained on day 5 revealed some regions in which pH decreased to approximately 6.6, while most of the leg had pH above 7.0. Regions of acidosis became significantly larger on day 8. To quantitatively characterize the change in tumor acidification, a 3D region of interest (ROI) that included

the whole thigh muscle and the tumor graft was defined by selecting ROIs in all 2D slices of sagittal MR images (red lines in Figs. 3c, 3d.

Quantitative analysis of pH_e data is presented in Figs. 3i to 3l. Fig. 3i shows the representative histograms of pH_e data for the mouse shown in Fig. 3. The overlaid histograms show that the distribution of pH_e was slightly shifted to lower pH on day 8. To confirm the reduction in pH_e of SCC VII tumors, we measured seven tumor-bearing mice in total on day 5 and 8. The tumor volumes, median pH_e values and acidic tumor volumes (pH_e < 7.0) for seven mice are summarized in Figs. 3j to 3l. The mean tumor volumes on day 5 and 8 were 0.70 cm^3 and 0.97 cm^3, respectively (two-tailed paired *t*-test, $P = 0.002$, $n=7$). The means of the median pH_e on day 5 and 8 were 7.11 and 7.04, respectively (two-tailed paired *t*-test, $P = 0.025$, $n=7$). Moreover, the means of acidic tumor volumes (pH_e < 7.0) on day 5 and 8 were 0.14 cm^3 and 0.38 cm^3, respectively (two-tailed paired *t*-test, $P=0.007$, $n=7$). There was no correlation observed between EPR signal intensity and the measured pH_e value (figure provided in Supporting Information; Fig. S3).

pH mapping of tumor xenograft mouse models.

The proposed method of 3D pH_e mapping for detection of extracellular acidosis was further validated using three types of tumor xenograft mouse models. We used the human-derived pancreatic ductal adenocarcinoma cells MIA PaCa-2, SU.86.86, and Hs766t. (Full details of animal preparation are given in Supporting Information.) It was previously shown that these tumor types exhibit different levels of oxygenation and pyruvate metabolism by EPR and hyperpolarized ^{13}C MRI.[27] Fig. 4a shows sagittal T_2-weighted MR anatomical images of tumor-bearing mouse legs with MIA PaCa-2, SU.86.86, and Hs766t tumor xenografts. All three tumors were similar in size on the day of the measurements; ROI volumes were 1.09, 1.11, and 0.99 cm^3 for MIA PaCa-2, SU.86.86, and Hs766t tumors, respectively. Corresponding maps of the EPR signal intensity and pH_e are shown in Figs. 4b and 4c. For the MIA PaCa-2 tumor xenograft, the EPR signal intensity was relatively homogeneous, indicating a uniform distribution of the spin probe inside the tumor. The observed pH_e in all regions of the tumor was above 6.8. In contrast, the SU.86.86 tumor xenograft exhibited a large area of low or no EPR signal, making it impossible to calculate pH at the center of the tumor (void area in pH_e map, Fig. 4c). Severe extracellular acidosis (pH_e 6.2–6.3) was observed in other regions of the tumor. For the Hs766t tumor, some areas of low EPR signal intensity were also observed (pH_e 6.5–6.6). Notably, the areas with low pH_e did not directly correlate with the EPR signal intensity, *i.e.*, spin probe concentration, in this tumor type. In total, three mice bearing MIA PaCa-2, two mice bearing SU.86.86, and two mice bearing Hs766t tumors were scanned. In all cases, results similar to those presented in Fig. 4 were obtained. The mean values of the median pH_e were 7.05 (MIA PaCa-2, $n=3$), 6.90 (SU.86.86, $n=2$), and 6.91 (Hs766t, $n=2$).

DISCUSSION

The functional resolution of pH is an essential aspect of our method of pH mapping. Since the spin probe loses its sensitivity to pH at pH values far from pK_a, the accuracy and the functional resolution of pH measurements depend on the pH value being measured. This

sensitivity dependence in pH measurements using R-SG was previously reported.[23,25] Our EPR-based pH mapping technique has optimal pH resolution around pK_a defined by the characteristics of R-SG and dR-SG. Since the pK_a of R-SG at 37 ºC is 6.60 pH units, the probe can cover the full biologically relevant range of pH_e in normal tissues (close to 7.4 pH units) and in acidic conditions (below 7.0 pH units and even down to ~6.0 pH units).

The transient increase in the concentration of the radical in the blood during EPR acquisitions should not have any significant harmful effect on the animal. For *in vivo* 3D pH mapping, we used a rather high dosage of the spin probe (10 mg or 0.6 mmol/kg body weight) injected intravenously over a period of 30 seconds. Assuming that mouse blood volume is approximately 1.5 mL, the peak concentration of the radical in the blood could reach ~10 mM.

Three-dimensional pH mapping was successfully performed within 7.5 min for a living mouse using a single bolus injection of dR-SG, as shown in Figs. 3 and 4. EPR signal kinetics of the R-SG spin probe measured *in vivo* in mouse tumors on day 5 and 8 after implantation of SCC VII cells are provided in Supporting Information (Fig. S4). On both occasions, the EPR signal kinetics were comparable; signal appeared immediately after the intravenous injection of the probe, reached a maximum after about 2 minutes and then gradually declined. The intensity of EPR signal was approximately 80% of its maximum 10 minutes after probe injection (Fig. S4). The 4D spectral-spatial EPR imaging acquisition was thus designed to acquire 3375 projections between 2 and 9.5 minutes post injection of the probe. The primary route of radical removal from the animal is likely its reduction to the corresponding hydroxylamine, followed by renal excretion. Supporting this hypothesis, a high concentration of the reduced form of dR-SG was detected in the mouse urine after the experiments (see Fig. S5). Using EPR imaging, we were able to generate 3D maps of extracellular pH and visualize the expansion of regions of acidosis with tumor development (Fig. 3). Murine squamous cell carcinoma SCC VII is a well-documented fast-growing tumor,[28] and is known to exhibit some regions of severe hypoxia and localized alterations in cellular glucose metabolism.[29] In previous EPR (1D) spectroscopy measurements, it was shown that the average pH_e of SCC VII tumors gradually decreased over 11 days post-implantation.[23] However, the spatial distribution of pH_e in tumors cannot be visualized by spectroscopic measurements. In all measured tumors, we observed a region of low EPR signal intensity. However, the T_2-weighted MR anatomical images revealed no clear structural peculiarities in the corresponding region (see Figs. 3d and 3f). Considering the intravenous route of dR-SG administration, the low EPR signal indicates low vascular delivery, which is most likely due to necrosis inside the tumor, but may also be caused by low angiogenesis, interstitial pressure, or other conditions.

The temperature dependence of pK_a is 0.017 pH units/ºC, as calculated from the difference in reported pK_a values at 23 and 37 ºC. This dependence is well below the functional resolution of our pH measurements (0.078 pH units). Therefore, small fluctuations in body temperature (typically between 36 and 37 ºC) during image acquisition should not significantly affect our pH mapping results.

In addition to the temperature dependence, the probe concentration in extracellular space in tumors may have an impact on the resultant pH_e values. For accurate pH_e measurements, it is essential to keep the probe concentration below the buffer capacity of the blood. To clarify this influence, the concentration of dR-SG in extracellular space should be experimentally verified, considering the kinetics and spatial distribution of the probe in the mice, but this is beyond the scope of the present work.

No correlation between the signal intensity and pH_e was observed (Fig. S3). The observed areas of extracellular acidosis were frequently located near the borders of weakly perfused tissue. This acidosis may be explained by the fact that tissue near the tumor periphery likely has better access to metabolic nutrients and thus a higher rate of glycolysis, while the cells deep inside the tumor may remain dormant. Interestingly, acidic pH_e near the tumor periphery was previously observed for rat gliomas measured by an MR spectroscopic imaging technique.[30]

Our proposed EPR imaging method for pH_e mapping also enabled the visualization of differences in extracellular acidosis for three types of human-derived pancreatic ductal adenocarcinoma xenografts. The human-derived cancer cells MIA PaCa-2, SU.86.86, and Hs766t were previously studied for glucose metabolism and oxygenation.[27] It was reported that the SU.86.86 tumor xenograft has high vascular density and a lower rate of pyruvate to lactate metabolic conversion *in vivo* than MIA PaCa-2 or Hs766t tumors.[27] In contrast, in our measurements, a very low EPR signal was detected inside the SU.86.86 tumor. Because the spin probe was injected intravenously and EPR measurements were performed within 10 minutes of injection, we believe that the EPR signal intensity distribution reflects how well the tumor tissue is perfused by the blood. In this context, the obtained data suggest that SU. 86.86 has relatively low blood supply. Furthermore, the SU.86.86 tumor demonstrated the strongest acidosis among all tumor xenografts. Some regions of low signal intensity and pronounced acidosis were also detected in the Hs766t tumor. In contrast, MIA PaCa-2 showed relatively high EPR signal throughout the whole tumor and exhibited only mild extracellular acidosis. According to reference,[27] the tumor cells of both MIA PaCa-2 and Hs766t have a high rate of proton production *in vitro* and rapidly convert pyruvate to lactate *in vivo*. Thus, the milder acidosis of MIA PaCa-2 tumors observed by EPR imaging in this study may be attributed to better perfusion of the tumor, faster proton removal by the blood and possibly more efficient mitochondrial respiration.

CONCLUSION

We demonstrated a method for EPR-based *in vivo* pH mapping of mouse tumors. The method is capable to quantitatively visualize the progress of tissue acidification during tumor growth and to distinguish different levels of extracellular acidosis in various tumor models. Monitoring of extracellular pH *in vivo* may offer a powerful tumor assessment tool for a variety of preclinical studies, in order to establish the metabolic profile of novel cancer tumor models and to develop new therapeutic strategies.

Supplementary Material

Refer to Web version on PubMed Central for supplementary material.

ACKNOWLEDGMENT

This work was supported in part by Japan Society for the Promotion of Science (JSPS) KAKENHI Grant number 26249057 (to H.H.), Japan Science and Technology Agency (JST)-PRESTO (to S.M.), Ministry of Education and Science of the Russian Federation, application no. 2017-220-06–7355 (to I.A.K.), and National Institutes of Health (NIH) Grants CA194013 and CA192064 (to V.V.K.). N.J.S. is a JSPS International Research Fellow.

REFERENCES

(1). Denko NC Nat. Rev. Cancer 2008, 8, 705–713. [PubMed: 19143055]

(2). Swietach P; Vaughan-Jones RD; Harris AL; Hulikova A Phil. Trans. R. Soc. B 2014, 396, 20130099.

(3). Corbet C; Feron O Nat. Rev. Cancer 2017, 17, 577–593. [PubMed: 28912578]

(4). Zhang X; Kin Y; Gillies RJ J. Nucl. Med 2010, 51, 1167–1170. [PubMed: 20660380]

(5). Helmlinger G; Yuan F; Dellian M; Jain RK Nat. Med 1997, 3, 177–182. [PubMed: 9018236]

(6). Gillies RJ; Liu Z; Bhujwalla Z Am. J. Physiol. Cell. Physiol 1994, 267, C195–C203.

(7). Schmid AI; Meyerspeer M; Robinson SD; Goluch S; Wolzt M; Fiedler GB; Bogner W; Laistler E; Kršśák M; Moser E; Trattnig S; Valkovič L Magn. Reson. Med 2016, 75, 2324–2331. [PubMed: 26115021]

(8). Chen LQ; Randtke EA; Jones KM; Moon BF; Howison CM; Pagel MD Mol. Imaging. Biol 2015, 17, 488–496. [PubMed: 25622809]

(9). Gallagher FA; Kettunen MI; Day SE; Hu DE; Ardenkjær-Larsen JH; Zandt R. i.; Jensen PR; Karlsson M; Golman K; Lerche MH; Brindle KM Nature 2008, 453, 940–943. [PubMed: 18509335]

(10). Düwel S; Hundshammer C; Gersch M; Feuerecker B; Steiger K; Buck A; Walch A; Haase A; Glaser SJ; Schwaiger M; Schilling F Nat. Commun 2017, 8, 15126. [PubMed: 28492229]

(11). Bobko AA; Eubank TD; Voorhees JL; Efimova OV; Kirilyuk IA; Petryakov S; Trofimiov DG; Marsh CB; Zweier JL; Grigor'ev IA; Samouilov A; Khramtsov VV Magn. Reson. Med 2012, 67, 1827–1836. [PubMed: 22113626]

(12). Samouilov A; Efimova OV; Bobko AA; Sun Z; Petryakov S; Eubank TD; Trofimov DG; Kirilyuk IA; Grigor'ev IA; Takahashi W; Zweier JL; Khramtsov VV Anal. Chem 2014, 86, 1045–1052. [PubMed: 24372284]

(13). Gallez B; Mäder K; Swartz HM Magn. Reson. Med 1996, 36, 694–697. [PubMed: 8916019]

(14). Sotgiu A; Mäder K; Placidi G; Colacicchi S; Ursini CL; Alecci M Phys. Med. Biol 1998, 43, 1921–1930. [PubMed: 9703055]

(15). Foster MA; Grigor'ev IA; Lurie DJ; Khramtsov VV; McCallum S; Panagiotelis I; Hutchison JMS; Koptioug A; Nicholson I Magn. Reson. Med 2003, 49, 558–567. [PubMed: 12594760]

(16). Khramtsov VV; Grigor'ev IA; Foster MA; Lurie DJ Antioxid. Redox Signal 2004, 6, 667–676. [PubMed: 15130294]

(17). Marchand V; Leveque P; Driesschaert B; Marchand-Brynaert J; Gallez B Magn. Reson. Med 2016, 77, 2438–2443. [PubMed: 27364733]

(18). Bobko AA; Eubank TD; Driesschaert B; Dhimitruka I; Evans J; Mohammad R; Tchekneva EE; Dikov MM; Khramtsov VV Sci. Rep 2017, 7, 41233. [PubMed: 28117423]

(19). Sato-Akaba H; Fujii H; Hirata H Rev. Sci. Instrum 2008, 79, 123701. [PubMed: 19123563]

(20). Sato-Akaba H; Kuwahara Y; Fujii H; Hirata H Anal. Chem 2009, 81, 7501–7506. [PubMed: 19645455]

(21). Komarov DA; Hirata HJ Magn. Reson 2017, 281, 44–50.

(22). Kawada Y; Hirata H; Fujii HJ Magn. Reson 2007, 184, 29–38.

(23). Goodwin J; Yachi K; Nagane M; Yasui H; Miyake Y; Inanami O; Bobko AA; Khramtsov VV; Hirata H NMR Biomed 2014, 27, 453–458. [PubMed: 24470192]

(24). Snedecor GW; Cochran WG Statistical Methods, 8th *edition;* Iowa State University Press: Ames, 1989; pp 83–106.

25. () Komarov DA; Dhimitruka I; Kirilyuk IA; Trofimiov DG; Grigor'ev IA; Zweier JL; Khramtsov VV Magn. Reson. Med 2012, 68, 649–655. [PubMed: 22162021]

(26). Gorodetsky AA; Kirilyuk IA; Khramtsov VV; Komarov DA Magn. Reson. Med 2016, 76, 350–358. [PubMed: 26301868]

(27). Wojtkowiak JW; Cornnell HC; Matsumoto S; Saito K; Takakusagi Y; Dutta P; Kim M; Zhang X; Leos R; Bailey KM; Martinez G; Lloyd MC; Weber C; Mitchell JB; Lynch RM; Baker AF; Gatenby RA; Rejniak KA; Hart C; Krishna MC; Gillies RJ Cancer Metab 2015, 3, 2. [PubMed: 25635223]

(28). Suit HD; Suchato C Radiology 1967, 89, 713–719. [PubMed: 6059611]

(29). Matsumoto S, Hyodo F; Subramanian S; Devasahayam N; Munasinghe J; Hyodo E; Gadisetti C; Cook JA; Mitchell JB; Krishna MC J. Clin. Invest 2008, 118, 1965–1973. [PubMed: 18431513]

(30). Provent P; Benito M; Hiba B; Farion R; López-Larrubia P; Ballesteros P; Rémy C; Segebarth C; Cerdán S; Coles JA; García-Martín ML Cancer Res 2007, 67, 7638–7645. [PubMed: 17699768]

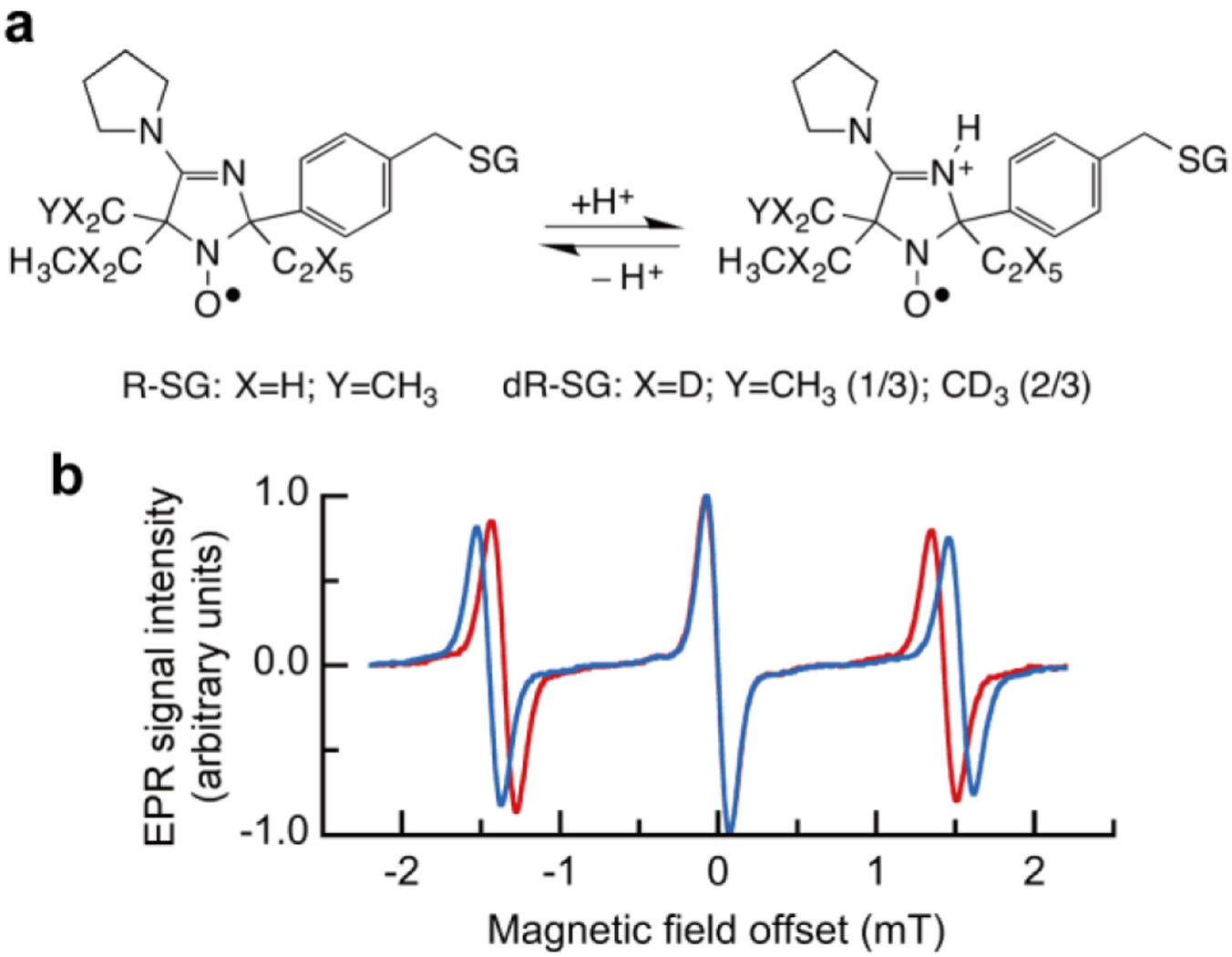

Figure 1.

pH-sensitive radical probe and its EPR spectra. (a) Chemical structures and scheme of protonation of pH-sensitive nitroxyl radical (R-SG) and its deuterium-enriched analog (dR-SG). (b) First-derivative EPR spectra of 2 mM dR-SG measured at 750 MHz in alkaline (pH = 10.0, blue line) and acidic (pH = 3.0, red line) solutions. SG stands for glutathione residue. Note, the central line of the spectra does not depend on pH.

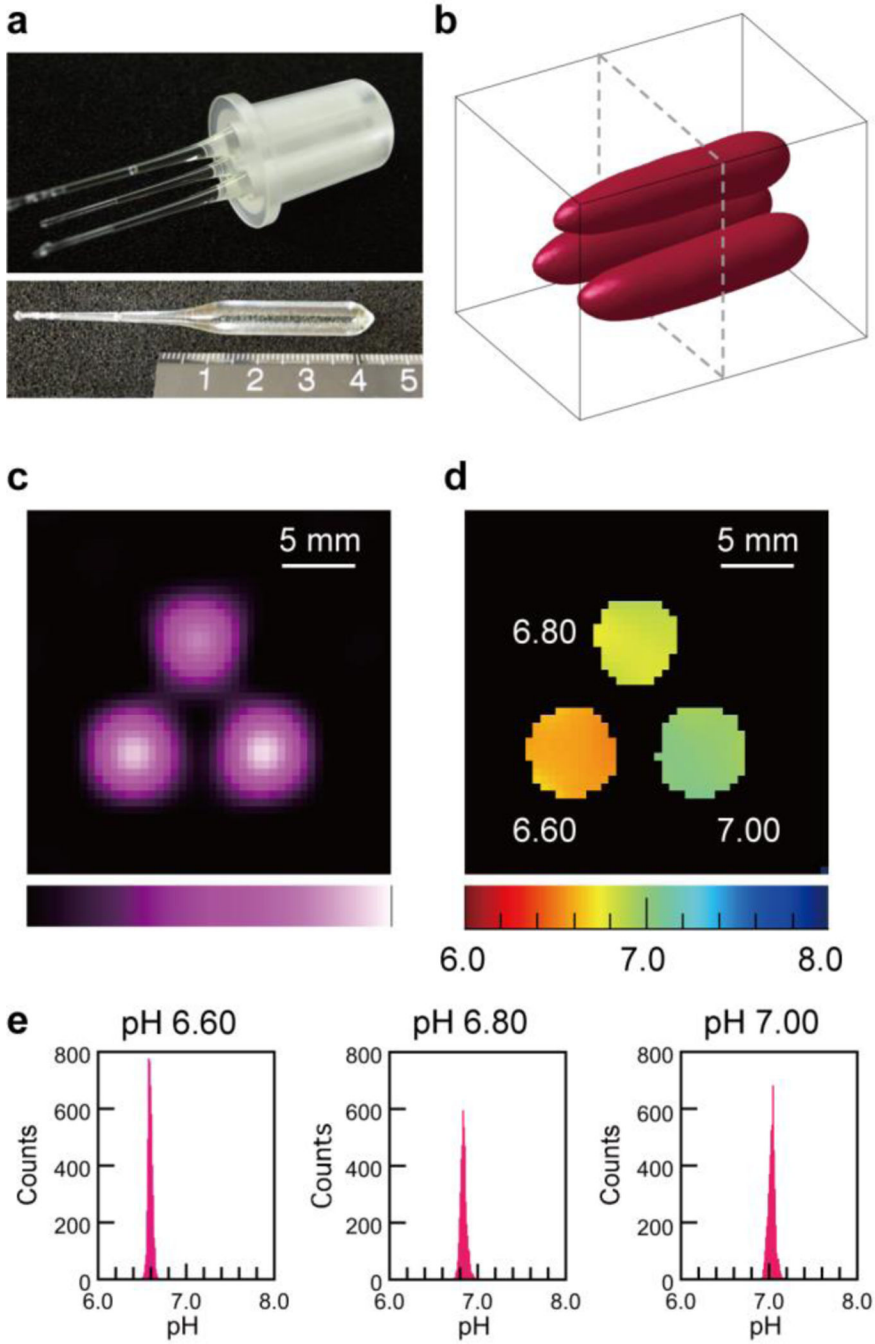

Figure 2.

Three-dimensional visualization and EPR characterization of the pH phantom. (a) Photograph of the phantom sample, consisting of three flame-sealed glass tubes (inner diameter 5.3 mm, volume ~0.7 mL) placed in a plastic holder (scale in cm). The tubes were filled with 2 mM solutions of R-SG in PBS with pH values adjusted to 6.60, 6.80, and 7.00. (b) 3D surface-rendered image of EPR signal intensity calculated with a 35% threshold: image matrix size 48 × 48 × 64, field-of-view 25.0 mm × 25.0 mm × 33.3 mm. (c) EPR signal intensity distribution, and (d) map of pH for the central slice of the 3D image

(indicated by dashed lines in (b)), shown with a 35% threshold of signal intensity and pH, respectively. (e) Histograms of pH for each of the three tubes. The measured pH values were 6.591 ± 0.025, 6.839 ± 0.035 and 7.029 ± 0.039 (mean ± standard deviation).

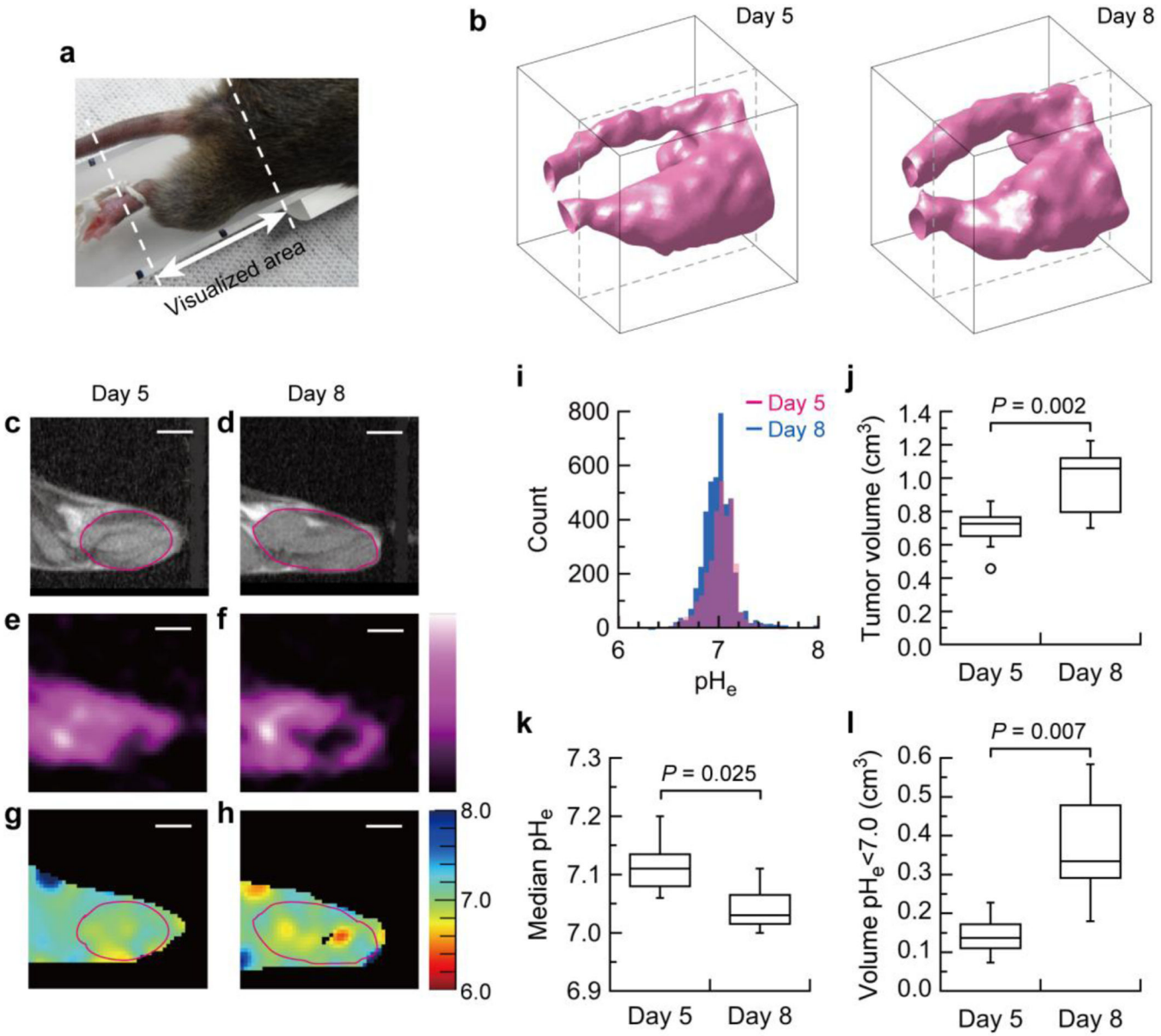

Figure 3.

Progress of acidification in an SCC VII tumor-bearing mouse leg during tumor growth. (a) Photograph of the mouse leg fixed on a plastic holder and (b) 3D surface-rendered images of EPR signal measured at day 5 and day 8 after tumor implantation. The image matrix size was 48 × 48 × 48, field-of-view 25.0 mm × 25.0 mm × 25.0 mm. (c) and (d) T_2-weighted proton MR anatomical images of the mouse leg in the sagittal plane, acquired at day 5 and 8, respectively, scaled and cropped to match the EPR images. (e, f) Representative slices of EPR signal intensity taken from the 3D data, and (g, h) corresponding maps of pH_e. The white scale bar on the images corresponds to 5 mm. (i) Representative histograms of voxel-wise pH_e data measured on day 5 (red) and 8 (blue) for a single mouse. Box-and-whisker plots of (j) the tumor volume, (k) the median pH_e, and (l) the acidic tumor volume (pH_e <

7.0) for $n = 7$ mice. The circle in (j) represents an outlier. A two-tailed paired t-test was used to determine statistical significance P.

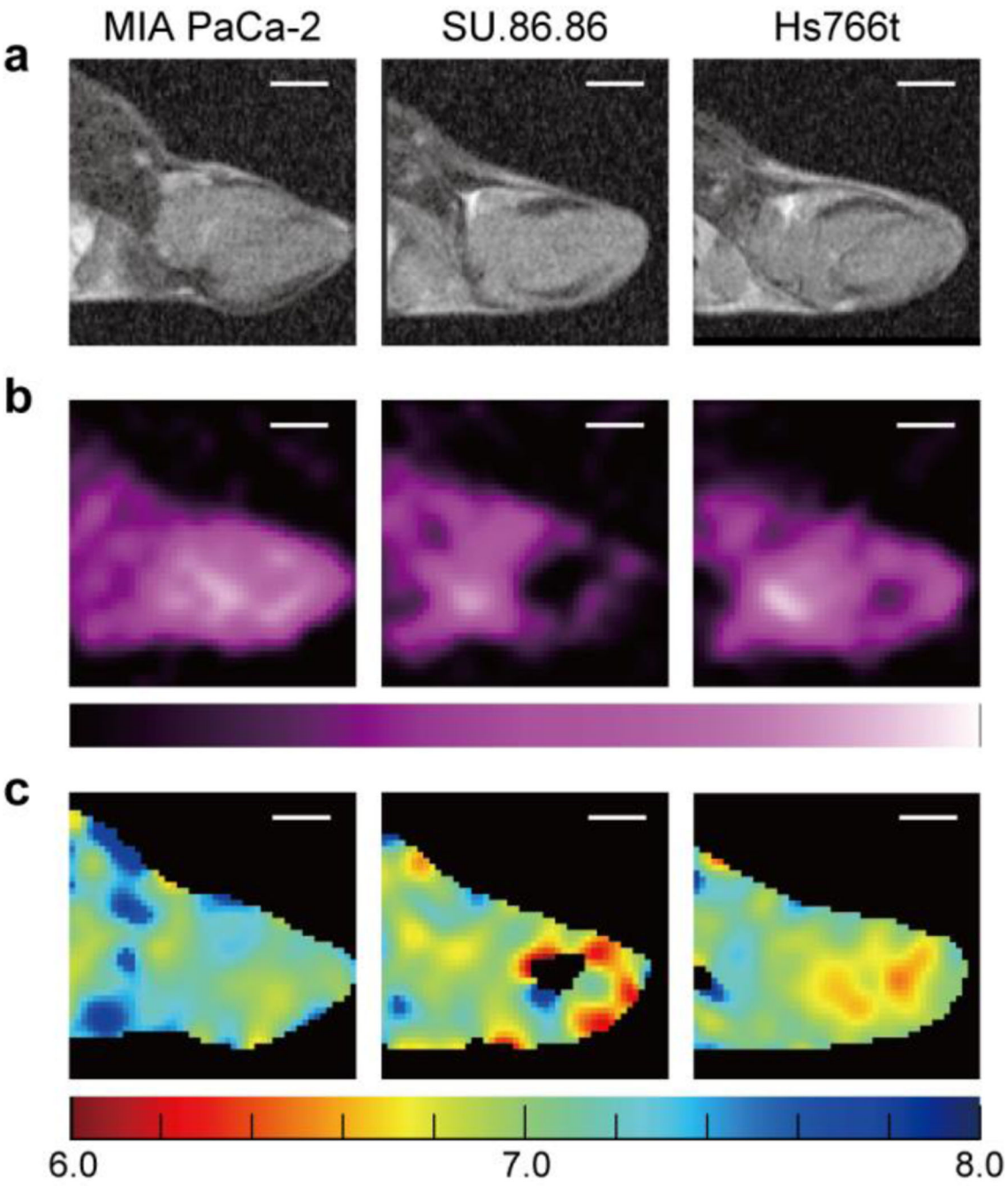

Figure 4.

Visualization of pH_e in mouse legs bearing the human-derived pancreatic ductal adenocarcinoma xenografts MIA PaCa-2, SU.86.86, and Hs766t. (a) Representative T_2-weighted MR anatomical images of tumor-bearing mouse legs in the sagittal plane, (b) corresponding slices of EPR signal intensity, and (c) maps of pH_e. The matrix size of the EPR images was 48 × 48 × 48, field-of-view 25.0 mm × 25.0 mm × 25.0 mm. MR images

were scaled and cropped to match the corresponding EPR images. The white scale bar on the images corresponds to 5 mm in all cases.